

Environmental Monitoring and Change Detection Using Dual-Stream Convolutional Networks with Fusion Techniques on Satellite Imagery

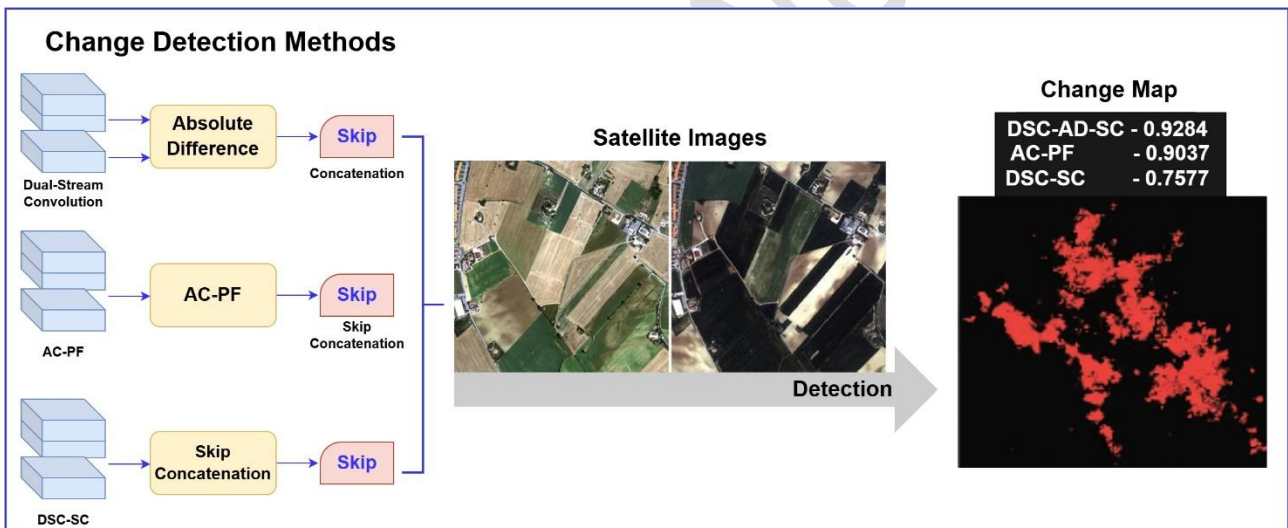
Aiswarya Jeevan^{1,*} and Amala Shanthi S²

¹Research Scholar, Department of Electronics and Communication Engineering, Noorul Islam Centre for Higher Education, Thuckalay, Kumaracoil, Tamil Nadu, India.

²Associate Professor, Department of Electronics and Communication Engineering, Noorul Islam Centre for Higher Education, Thuckalay, Kumaracoil, Tamil Nadu, India.

*Corresponding Author: Aiswarya Jeevan; E-mail: aiswaryajeevan572@gmail.com

Graphical Abstract:



21 **ABSTRACT**

22 Change monitoring on the Earth's surface has become vital for understanding environmental
23 processes and developing sustainable resource management decisions. For numerous applications,
24 ranging from mapping urban sprawl to assessing the impacts of natural hazards, approximating
25 environmental damage, and analyzing forest loss, precision in change detection (CD) methods is
26 paramount. This work entails a thorough examination of enhanced CD techniques that are particularly
27 designed to improve accuracy when detecting changes in satellite data. The three methods that are
28 examined include Dual-stream convolution with absolute difference of skip concatenation (DSC-AD-
29 SC), absolute convolutional prior fusion (AC-PF), and dual-stream convolution with skip
30 concatenation (DSC-SC). To optimize CD accuracy and effectiveness in monitoring changes in
31 geographical features over time, each method employs specialized convolutional operations. The
32 research analyzes environmental changes over time using Onera satellite change detection dataset. A
33 data augmentation step is introduced to the pipeline to enhance dataset diversity and model
34 robustness. Performance is compared using multiple parameters, and the results indicate the highest
35 Dice Similarity Score of 0.9284 for the DSC-AD-SC model, followed by AC-PF at 0.9037 and DSC-
36 SC at 0.7577. The proposed methods are found to be effective in enhancing change detection
37 performance and yield informative measures for use in environmental monitoring and disaster
38 response applications.

39 **Keywords:** Change detection, Skip concatenation, Environmental dynamics, geographical features,
40 Environmental monitoring.

41

42

43

44

45

46

47 **1. Introduction**

48 Change detection is an important method for detecting surface change and finds numerous
49 applications in catastrophe evaluation, agricultural monitoring, city planning, ecological monitoring,
50 and map revision. Innovative change detection methods have recently centered on integrated artificial
51 intelligence (AI) technology (Shi et al., 2020). Urbanization, agriculture, and forest removal are some
52 human operations that can significantly disturb water supplies. Between 1972 and 2017, the
53 proportion of the watershed that consisted of cultivated land and agroforestry increased from 24.2%
54 to 62%. Natural vegetation has lost a large amount of land to these two land use types. For the entire
55 watershed, 74.34% of its land cover transformed in 45 years (Degife et al., 2019). Policy initiatives
56 targeted at raising agricultural output remain one of the most effective methods to relieve strain on
57 Nigeria's increasingly restricted land resources while also conserving natural ecosystems (Arowolo
58 and Deng, 2018). Change detection plays an important role, environmental monitoring, and detecting
59 land use and land cover change. Remote sensing satellites gather satellite images with varied
60 resolutions and utilize them to identify changes (Asokan and Anitha 2019). Figure 1 compares the
61 satellite and aerial images of the same location.



62

63 **Figure 1.** Satellite image and aerial image of the same area

64 Remote sensing provides extensive geographical and spectral resolution for monitoring
65 desertification, agroforestry, rangelands, soil, water, watersheds, crop use patterns, urban expansion
66 of agricultural land, and monitoring of climate variations and their effects on agriculture. Several
67 programs/projects in India, including FASAL, CAPE, NNRMS, NADAMS, IMSD, CHAMAN, and

68 others, are successfully supporting agricultural management (Kumar et al., 2022). Principal
69 component analysis (PCA), iteratively reweighted-multivariate alteration detection (IRMAD), and
70 change vector analysis (CVA) were used to create three change intensity images. These three intensity
71 images were utilized to construct various binary PBCD maps, which were then merged with the
72 segmented image using wDST to produce the OBCD map (Han et al., 2020). The proposed change
73 detection method was also tested utilizing very high resolution (VHR) satellite images for binary
74 class change detection to map a natural disaster-impacted area, and the results were evaluated against
75 reference data from the Federal Emergency Management Agency (FEMA) (Liu et al., 2021). The
76 training regions are automatically generated using the geographical information system (GIS)
77 database. Even if the problems mentioned above are addressed, there remain a lot of inherent issues
78 in RS datasets that still have not been tackled due to evolving requirements and diverse data, such as
79 heterogeneous data, multiresolution images, and global knowledge of large-scale and high-resolution
80 images (Walter, 2004; Shafique et al., 2022).

81 Kalinicheva et al., (2020) introduced an unsupervised method of satellite image (SITS) change
82 detection and clustering. Bitemporal change masks were designed for every next image pair in their
83 system based on neural network autoencoders. The system that incorporated graph-based method
84 with unsupervised feature learning via a neural network was independent of the duration and temporal
85 resolution of the SITS. They also highlighted the issue of the algorithm having difficulty in
86 interpreting changes that occurred over different time periods, particularly the requirement that a
87 graph must be constructed to screen for objects.

88 Song et al., (2020b) proposed an object-based change detection for high-resolution satellite images.
89 The process consists of two main steps. Initially, Objects were constructed based on unsupervised
90 CD methods to train the network, which comprised LSTM layers. To identify changes in satellite
91 images, Sefrin et al., (2020c) merged a fully convolutional neural network (FCN) with a LSTM
92 network. Whereas the FCN was limited to processing input data with one temporal dimension, the

93 hybrid FCN-LSTM method employed sequential information for multitemporal data. Both variable
94 and fixed sequences were supplied and fixed sequences as training inputs for the combination method.
95 Two change detection techniques were tested by Goswami et al., (2022) with a decision tree
96 algorithm. To compare post-classification, employing the separability matrix, the first technique
97 utilized the decision tree algorithm in order to detect individual images. The second method, image
98 differencing, separated the pixels that were changed from those that remained unchanged through the
99 use of the corner method. The limitations of the study were that algorithm they employed was
100 relatively outdated and the technique was evaluated on a small dataset. Khankeshizadeh et al., (2022)
101 proposed a U-Net deep neural network for forest change detection.

102 A novel difference image was developed to allow for more accurate discrimination between changed
103 and unchanged regions. R2U-Net was employed in order to discriminate the EFFDI among areas that
104 had changed and those that were unchanged since it preserved geometric shapes more than previous
105 versions of U-Net. Kalinaki et al., (2023) improved the architecture of U-Net using attention methods
106 to emphasize important features and residual links to achieve smooth information passing and
107 gradient propagation. The capability of extracting features accurately enhanced the computer
108 performance compared to Standard U-Net and Attention U-Net. The design choices of the method
109 lead to issues like inadequate feature extraction, lost spatial context, and limited adaptability, all of
110 which would ultimately compromise the accuracy and reliability of the system. Difference-aware
111 attention network was proposed by Mei et al., (2023) for dual-temporal satellite data-based
112 simultaneous building localization and multi-level change detection. The authors developed paired
113 features to activate change-sensitive channels and learn the global change pattern. In summary, while
114 these U-Net-based extensions focus on improving feature extraction or spatial attention, they do not
115 explicitly exploit feature-level absolute differences between temporal image pairs, which is a key
116 aspect addressed in the proposed approach.

117 For urban flood detection, Tanim et al., (2022) presented an unsupervised machine learning
118 framework that integrates the fuzzy rules, Otsu algorithm, and iso-clustering techniques. According

119 to the results of the performance evaluation of the support vector machine, random forest, accuracy
120 measures of 0.87 and 0.69. A study comparing the effectiveness of current deep learning methods in
121 satellite imagery was carried out by Tahir et al., (2022). They used convolutional neural network-
122 based frameworks, such as satellite imagery multiscale rapid detection, and the You Only Look Once
123 (YOLO) method, to perform object detection on a dataset of satellite imagery.

124 While many change detection methods based on deep learning have been proposed, these approaches
125 have limitations. Existing approaches are mostly based on a single stream or loosely coupled dual-
126 stream architectures, which do not explicitly model the feature-level differences between bi-temporal
127 images. While U-Net-based variants performed better in spatial localization, they focus more on
128 feature fusion and less on temporal differences. While attention-based models are good at selecting
129 influential features, they come with added computational complexity, and subtle changes in the
130 environment. The findings suggest that developing architectures that directly emphasize temporal
131 differences while ensuring spatial consistency is warranted, leading to the proposal of dual-stream
132 models in this study.

133 Change detection datasets lack diversity due to frequent limitations on geographic location, seasonal
134 variations, or specific imaging conditions. This affects the model's generalizability across several
135 environments and time periods. Therefore, there should be larger and more comprehensive datasets
136 that reflect a wider variety of geographical and temporal changes. Handling VHR data is another
137 issue. The pixel-based change detection methods are unsuitable due to the computational
138 requirements and radiometric discrepancy of VHR data. Although object-based approaches yield
139 improved accuracy, research must still establish techniques capable of appropriately handling high-
140 resolution data without degrading output. Most change detection algorithms are not compatible with
141 other sensors or resolutions, as they are generally designed for a specific sensor or resolution. Another
142 domain that requires enhancement is the use of multimodal data. In most of the existing approaches,
143 while only spectral information from optical/SAR images is employed, there is an opportunity to
144 study multimodal approaches employing extra data sources like LiDAR, multispectral/hyperspectral

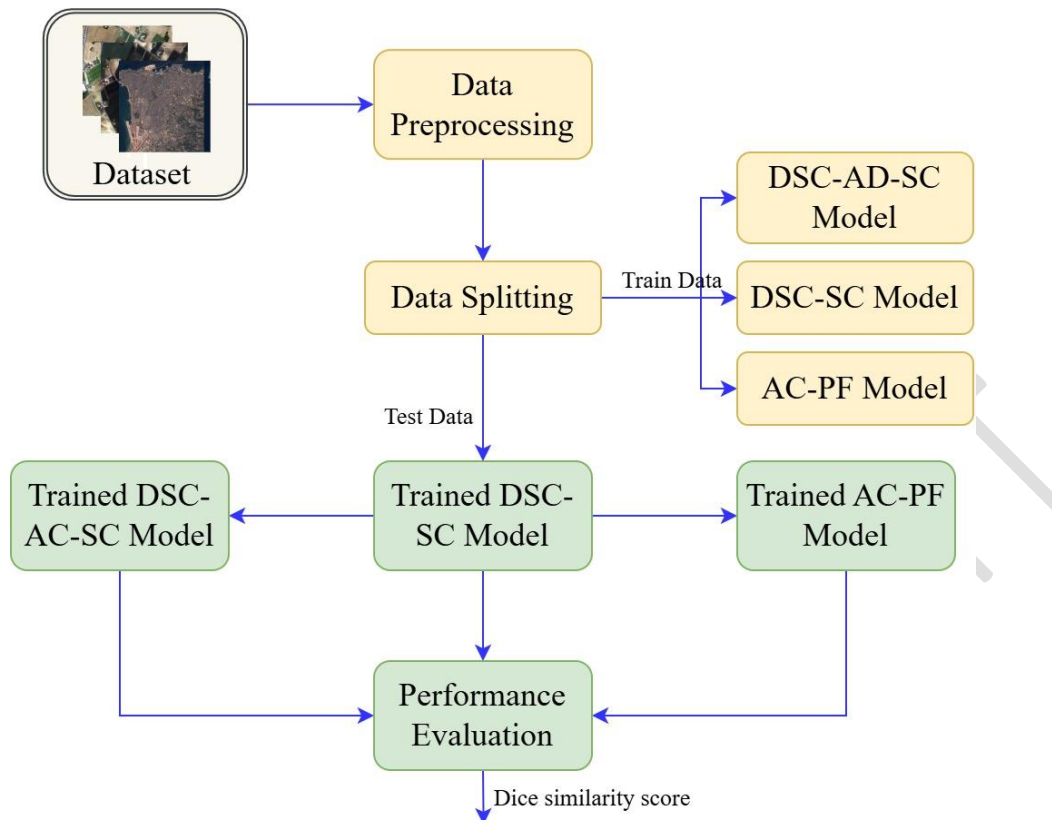
145 images. Eventually, there is little inquiry into sophisticated structures. Many existing methods utilize
146 conventional DL models, which miss the opportunity for more complex designs, such as Self-
147 Supervised Learning, Dual-Stream Networks, as well as attention processes. Better satellite analysis
148 architectures can detect more complex temporal and spatial correlations in satellite images, resulting
149 in better interpretation and detection of changes. This means that improving satellite image change
150 detection in these aspects can enhance its scalability and reliability. This will allow its use for more
151 applications such as disaster response and management, environmental monitoring, urban planning.

152 The major objectives of the study are as follows:

- 153 • To conduct a comprehensive evaluation of various change detection techniques, including
154 dual-stream convolution with absolute difference of skip concatenation, absolute
155 convolutional prior fusion, and DSC-SC, to understand their effectiveness and efficiency in
156 detecting changes in satellite imagery.
- 157 • To assess and compare the performance of each change detection method using standardized
158 evaluation metrics, namely Dice Similarity Score.

159 **2. Materials and Methods**

160 As shown in Figure 2, this study examines several change detection methods, with a specific focus
161 on the DSC-SC method, absolute difference-based convolutional fusion, and a dual-stream
162 convolutional network without skip concatenation. The strategies are utilized on satellite images
163 acquired at different time intervals to observe the changes in features. All the architectures aim to
164 improve the accuracy of change detection through different feature fusion methods. Their advantages
165 and disadvantages are subsequently examined. Data augmentation is used to increase dataset diversity
166 to increase robustness. Finally, standard performance metrics are used to assess the effectiveness of
167 the methods proposed.



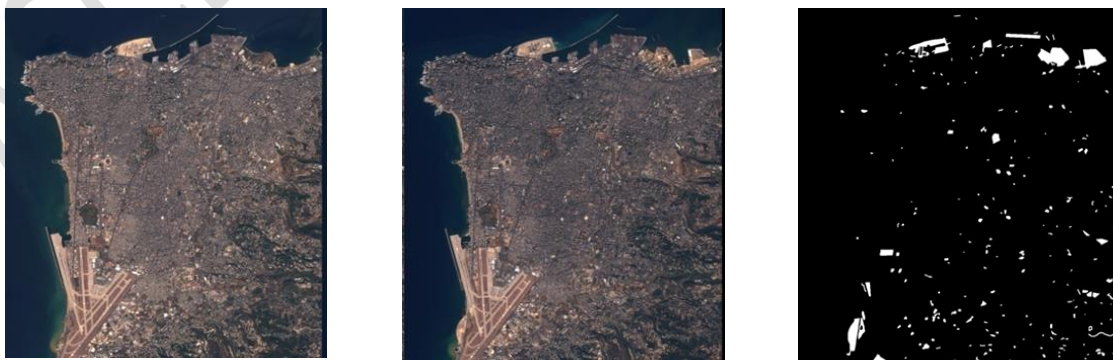
168

169

Figure 2. Block diagram of the Proposed approach

170 2.1 Dataset

171 The proposed study uses the Onera Satellite Change Detection Dataset which serves as a valuable
 172 resource for satellite image change detection research. The dataset includes geographical areas in
 173 Brazil, the USA, Europe, the Middle East, and Asia. The dataset includes 24 pairs of multispectral
 174 images captured by the Sentinel-2 satellites at during the period 2015–2018. A sample image from
 175 the dataset is shown in Figure 3. The dataset contains 13-band multispectral images in each pair.



176

Figure 3. Sample image from the dataset

177 The dataset is accompanied by pixel-level ground truth masks for the changes, focusing on
 178 urbanization. Algorithms can therefore be developed and evaluated for detecting changes.

179 This study uses all 13 spectral bands of the Sentinel-2 imagery to fully exploit the multispectral
180 information for change detection. These bands enhance accurate spectral and spatial measurement
181 throughout the visible, near-infrared and shortwave infrared wavelengths. They can be used for
182 assessing urban growth, vegetation cover and other land-use changes. Using all available bands
183 allows for the use of a richer feature space and helps the model detect smaller changes in the
184 environment.

185 *2.2 Data Preprocessing and Augmentation*

186 In satellite image analysis, data preprocessing has been widely applied to enhance data consistency
187 and improve feature learning by removing noise and overcoming spatial variations. This study
188 follows the following preprocessing steps namely normalizing spectral bands and bi-temporal images
189 alignment in order to achieve pixel-wise. In order to increase the diversity of the training dataset and
190 make the model more robust, augmentation techniques such as rotation, flipping, and minor spatial
191 alterations are applied as the number of labeled satellite image pairs is limited.

192 *2.3 Model Development*

193 To enhance clarity and accessibility, the workflow of the methodology is clearly explained step-by-
194 step, as well as the role of each architectural component in the change detection process. This dual-
195 stream design allows simultaneous feature extraction from bi-temporal images using shared weights
196 to learn high-quality feature representations. Approaches to feature fusion are implemented at varied
197 stages to focus on temporal differences, thus enhancing sensitivity to minor environmental changes
198 as well as changes. This clarification has been structured for a better comprehension of the proposed
199 methods so that researchers in the fields of remote sensing and deep learning.

200 The proposed work provides a comprehensive analysis of various change detection techniques. This
201 analysis is based on three key methods. They are: dual-stream convolution with absolute difference
202 of skip concatenation, absolute convolutional prior fusion, and DSC-SC. These approaches are
203 applied to satellite imagery to detect and evaluate changes in geographical features over time.

204 *2.3.1 Change detection using Absolute Convolutional Prior Fusion (AC-PF) model*

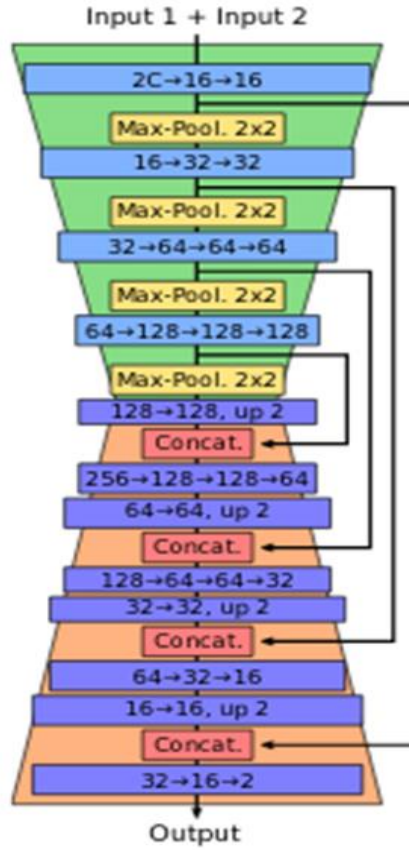
205 The AC-PF model is designed as an adaptation of the well-known U-Net architecture. This model
206 operates on two input satellite images (“before” and “after”), which are chipped into smaller patches
207 of size 96×96 to ensure that the input is effectively transformed into manageable patches. The choice
208 of a 96×96 patch size represents a balance between preserving sufficient spatial context for
209 meaningful change detection and maintaining computational efficiency during model training. This
210 patch size is large enough to capture localized environmental changes while allowing efficient batch
211 processing on limited GPU resources. The ultimate goal of the AC-PF model, as shown in Figure 4,
212 is to produce one output image, highlighting regions of change by comparing the two input images
213 through a semantic segmentation approach.

214 The AC-PF model retains the foundational encoder-decoder structure of U-Net but incorporates
215 several adjustments to better suit the available training data and to improve computational efficiency.
216 This results in a more comprehensive understanding of the changes between the two images. The
217 encoder part of the network involves several layers of convolutional operations followed by max-
218 pooling. The convolutional operations are mathematically represented in Equation (1).

$$219 \quad Z^{(l)} = f(W^{(l)} * Z^{(l-1)} + b^l) \quad (1)$$

220 Where the feature map at layer l is denoted by $Z^{(l)}$, $W^{(l)}$ are the learned weights (filters) of the
221 convolution, the output from the previous layer is denoted by $Z^{(l-1)}$, b^l represents the bias term, f is
222 the activation function, and $*$ denotes the convolution operation. The max-pooling operation is
223 performed after every convolution block to reduce the spatial dimensions and retain only the most
224 prominent features. Mathematically, max pooling is described as per Equation (2).

$$225 \quad P^{(l)}(i, j) = \max\{Z^{(l)}(i + x, j + y) : 0 \leq x, y < n\} \quad (2)$$



226
227 **Figure 4.** Architecture of the AC-PF model

228 Where $P^{(l)}(i, j)$ represents the pooled output, and n is the size of the pooling window. This process
229 reduces the resolution of the feature maps while preserving the most important information. In the
230 decoder portion, the model applies more sampling layers to increase the spatial dimensions of the
231 feature maps. By concatenating the feature maps, upsampling is achieved from the encoder, which
232 brings in more detailed information from the earlier layers. The up-sampling operation is
233 mathematically represented as per Equation (3).

$$234 \quad Z_{up}^{(l)} = \text{Upsampling}(Z^{(l)}) \quad (3)$$

235 Where $Z_{up}^{(l)}$ represents the upsampled feature map at layer. The upsampling and concatenation steps
236 ensure that information lost during the downsampling process is recovered, enabling the network to
237 make more precise predictions. The concatenation is represented as per Equation (4).

$$238 \quad Z_{concat} = \text{Concatenate}(Z_{encoder}, Z_{decoder}) \quad (4)$$

239 Through the rest of the convolutional layers, this is passed to produce the final output image
240 highlighting the regions of change between two images. The segmentation map is the outcome of the

241 AC-PF model that predicts changes accurately in the two satellite images. Tuning the
242 hyperparameters properly improves model performance, allowing the model to generalize better with
243 unseen data and achieve the best results. The values of the hyperparameters used in AC-PF model are
244 given in Table 1.

245 **Table 1.** Hyperparameters in the AC-PF model

Parameters	Values
Loss	Binary cross entropy
Epoch	50
Batch size	2
Activation	ReLU, Sigmoid
Optimizer	Adam

246

247 2.3.2 Satellite change detection using Dual-Stream Convolution with Skip Concatenation

248 The DSC-SC model is a two-stream encoder-decoder architecture that takes two images as input for
249 a change detection task and produces an output of one segmented image. The model illustrated in
250 Figure 5 is derived from the U-Net architecture (Ibtehaz and Rahman 2020), although with a new
251 arrangement of skip connections which combines features from both streams at the decoding stage
252 for accurate class predictions with sharp boundaries.

253 The encoder part of the DSC-SC model is divided into two parallel streams with the same structure
254 and shared weights. The two streams process one input each independently (“before” and “after”).
255 By sharing weights, both streams extract similar types of features from the two input images, making
256 the architecture computationally efficient while allowing it to capture shared features across the two
257 images. The convolutional operation in the shared encoder is defined as per Equation (5).

$$258 \quad F = \Phi(I) = W * I + b \quad (5)$$

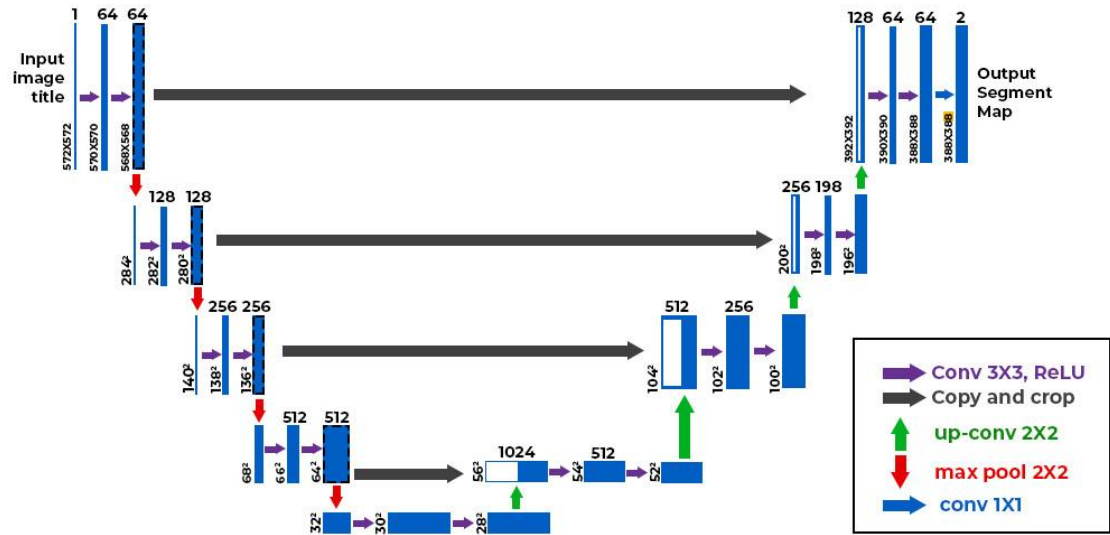


Figure 5. Basic U-Net architecture

Where the feature map generated from the encoder (the same for both streams) is represented by F is, W is the shared convolutional filter weights, I is the input image, and b is the shared bias term. Each branch includes additional branch-specific convolutional layers, as represented in Equation (6).

$$F_{branch} = \Psi(F) \quad (6)$$

Where F_{branch} is the feature map after branch-specific processing (which differs for each stream), Ψ denotes the branch-specific convolutional layers. The convolutional layers in each stream progressively extract higher-level features, while max pooling layers reduce the spatial resolution of the feature maps, retaining the most prominent features in each stream. The max pooling operation is defined as per Equation (7).

$$P(i, j) = \max\{F(i + x, j + y) : 0 \leq x, y < n\} \quad (7)$$

Where n is the size of the pooling window and the concatenation is denoted in Equation (8). Figure 6 illustrates the max pooling operation, by selecting the maximum value within a specified window, it effectively downs sampling the input while retaining the most significant features for subsequent processing.

$$X_{concat} = [S_{branch 1}, S_{branch 2}] \quad (8)$$

Where X_{concat} is the concatenated feature map, $S_{branch 1}$ and $S_{branch 2}$ are the skip connections from branches 1 and 2, respectively.

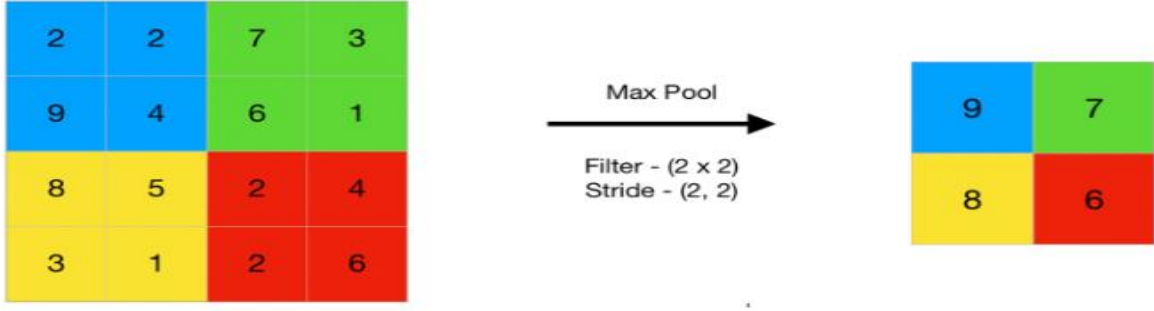


Figure 6. Max pooling operation illustration

278

279

280 This concatenation preserves both low-level features and high-level information, resulting in a richer
 281 feature representation. The decoder incorporates the concatenated skip connections from both streams
 282 along with up-sampled feature maps from the previous decoding layer. The up-sampling operation
 283 enlarges the feature maps to restore the spatial resolution, making it easier for the network to predict
 284 fine details in the output segmentation mask. The up-sampling operation is denoted in Equation (9).

$$285 \quad U = \text{Upsample}(F_{\text{decoder}}) \quad (9)$$

286 Where U is the up-sampled feature map from the decoder. The upsampled feature map is then
 287 concatenated with X_{concat} and passed through additional convolutional layers in the decoder, as
 288 represented in Equation (10).

$$289 \quad D = \Omega(U \oplus X_{\text{concat}}) \quad (10)$$

290 Where D is the feature map after processing in the decoder, \oplus denotes the element-wise addition,
 291 and Ω are the decoder layer parameters. The final stage of the decoder processes the combined feature
 292 maps through additional convolutional layers ' Ω ' to refine the output and predict the segmentation
 293 mask. The segmentation mask identifies changes between the two input images and assigns class
 294 probabilities for each pixel. The segmentation mask is generated using a sigmoid function to convert
 295 the final layer's output into probabilities, defined as per Equation (11).

$$296 \quad M_i = \text{sigmoid}(\Omega'(D))_i = \frac{\exp((\Omega'(D))_i)}{\sum_j \exp((\Omega'(D))_j)} \quad (11)$$

297 To a specific class, M_i is the predicted probability for pixel i , $\Omega'(D)_i$ is the output of the final
 298 convolutional layer for pixel i , the sigmoid function ensures the output is bounded between zero and
 299 one, allowing the model to predict whether each pixel belongs to the change or not. Table 2 outlines

300 the hyperparameters utilized in the DSC-SC model, providing detailed values and configurations
 301 employed during the training.

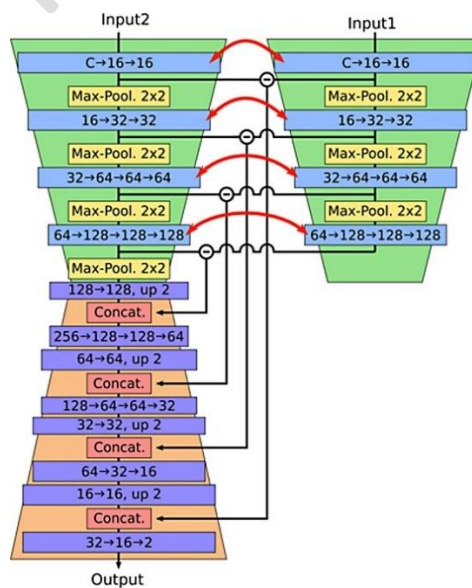
302 **Table 2.** Hyperparameters in the DSC-SC model

Parameters	Values
Loss	Binary cross entropy
Epoch	50
Learning rate	0.0001
Batch size	2
Activation	ReLU
Optimizer	Adam

303

304 2.3.3 Proposed Dual-Stream Convolution with Absolute Difference of Skip Concatenation

305 The DSC-AD-SC model as shown in Figure 7 is an extension of the previous DSC-SC architecture,
 306 specifically designed for tasks requiring the comparison of two input images, such as change
 307 detection. The DSC-AD-SC model inputs two images (“before” and “after”) and outputs a single
 308 image, which is a segmentation mask representing changes between the two images. Similar to the
 309 previous method, the input images are divided into 96 x 96 chips for processing.



310

311 **Figure 7.** Block schematic of the Proposed architecture

312 The novel aspect of the proposed model is in the treatment of skip connections. In particular, at the
 313 decoding stage, the absolute difference in the skip connections from both streams is computed and
 314 concatenated. An identical weight encoder is used in the dual stream architecture where two encoder
 315 streams encode features jointly. This is the encoding stage of the DSC-AD-SC model. The stream of
 316 processing one of the two input images (“before” and “after”) ensures that the features from the
 317 images are extracted consistently. The shared convolutional encoder function is defined as per
 318 Equation (12).

$$319 \quad F = \Phi(I) = W * I + b \quad (12)$$

320 Where the feature map generated by the shared encoder for both branches is represented by F , W
 321 represents the shared convolutional filter weights, I is the input image (before or after), and b is the
 322 shared bias term. Each stream includes additional branch-specific convolutional layers for further
 323 processing of the shared feature map. This branch-specific processing is defined as per Equation (13).

$$324 \quad F_{branch} = \Psi(f) \quad (13)$$

325 Where F_{branch} is the feature map after branch-specific convolution operations, Ψ represents the
 326 parameters of the branch-specific convolution layers. This step ensures that while the two streams
 327 share initial feature extraction operations, they can adapt their feature representations to capture
 328 specific characteristics of the “before” and “after” images.

329 Rather than just concatenating skip connections of both streams (as in the case of the DSC-SC model),
 330 the skip connections of the two branches are computed as their absolute difference by the DSC-AD-
 331 SC model. This method highlights the differences in the features learned from the “before” and “after”
 332 images, thus making the model more sensitive to change. The skip connection operation is
 333 represented as per Equation (14).

$$334 \quad S_{diff} = |S_{branch1} - S_{branch2}| \quad (14)$$

335 Where S_{diff} represents the absolute skip connection difference between branch 1 and branch 2,
 336 $S_{branch1}$ and $S_{branch2}$ represent skip connections from the two respective encoder streams. This
 337 operation makes the model concentrate on areas where the two images are not the same, so it is highly

338 appropriate for change detection applications. The absolute skip connections are concatenated with
 339 upsampled decoder features. The decoder of the DSC-AD-SC model is based on the general encoder-
 340 decoder architecture. The decoder's upsampled feature maps are merged with the absolute difference
 341 of skip connections at each step of decoding. The up-sampling operation is denoted as given by
 342 Equation (15).

$$343 \quad U = \text{Upsample}(F_{decoder}) \quad (15)$$

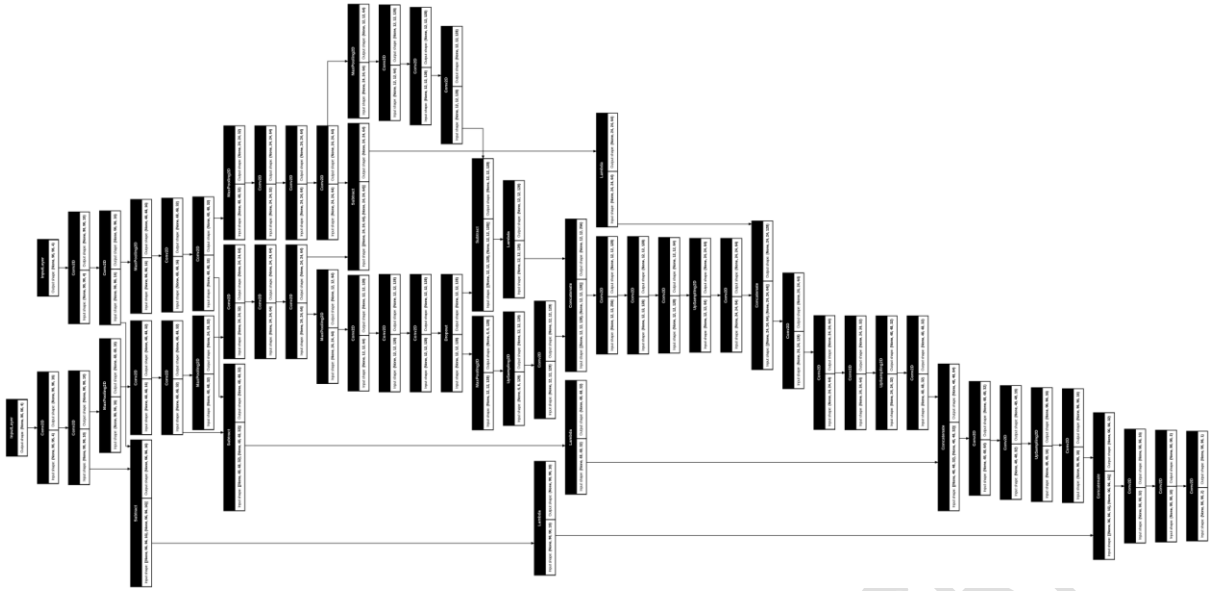
344 Where U is the upsampled feature map from the decoder. The up-sampled feature map is concatenated
 345 with the absolute difference of skip connections to form a more enriched feature representation for
 346 the decoding process as indicated per Equation (16).

$$347 \quad X_{concat} = [U, S_{diff}] \quad (16)$$

348 Where X_{concat} is the concatenated feature map consisting of the upsampled decoder features and the
 349 absolute difference of the skip connections. This combined feature map is further processed through
 350 additional convolutional layers in the decoder. In the final stage of the decoder, the combined feature
 351 maps are passed through additional convolutional layers to refine the output and generate the
 352 segmentation mask. This mask assigns class probabilities (foreground or background) to each pixel,
 353 representing areas of change between the input images. The final prediction is generated using a
 354 sigmoid function as per Equation (17).

$$355 \quad M_i = \text{sigmoid}(\Omega'(X_{concat}))_i = \frac{\exp((\Omega'(X_{concat}))_i)}{\sum_j \exp((\Omega'(X_{concat}))_j)} \quad (17)$$

356 Where M_i is the predicted probability (indicating change), Ω' represents the final convolutional layers
 357 in the decoder, the sigmoid function ensures that the output is a probability distribution, with values
 358 between 0 and 1. Figure 8 depicts the model architecture of the DSC-AD-SC model, showcasing the
 359 layers and structural components that contribute to its performance in addressing the specified task.



360

361

Figure 8. Model architecture of the DSC-AD-SC model

362

The proposed model, DSC-AD-SC, efficiently extracts and combines spatial features from both inputs for improved binary classification performance. The design is initiated with two input layers that each accept sequences with dimension (96, 96, 4). In addition to this, there are several convolutions and poolings performed per input branch, which ensures that the model operates efficiently, while capturing essential features. Initially, the model consists of two repeated Conv2D layers. The number of filters is 16, with a size of 3×3. Moreover, ReLU is the activation function used. After that, a MaxPooling layer is applied to downsample the feature maps.

369

Starting from the fusion layer, the model executes up-sampling using Conv2D layers that feature 128, 64, and 32 filters, which help restore image details. The output or final layer is a Conv2d layer with a single filter and the sigmoid activation, making a binary prediction. Essentially, this allows the model a probability score to indicate the classification for each input sequence. The hyperparameters of DSC-AD-SC model mentioned in the Table 3 show the different values used in the training and optimization.

375

Algorithm 1: *DSC_AD_SC Model for satellite Image change detection*

376

Input: Dual input image data $X_1, X_2 \in R^{H \times W \times C}$ where H is the height, W is the width, C is the number of channels.

377

378

Output: Predicted segmentation mask with $Y \in R^{H \times W \times 1}$ with values between 0 and 1.

379 *Step 1: Data preparation*

380 *Input initialization: Load the two inputs X_1, X_2 into the model with shape (96,96,4)*

381 *Step 2: Define the model*

382 ➤ *CNN Branch 1*

383 • *Apply two 2D convolutional layers with 16 filters, each with a 3×3 kernel and ReLU*
384 *activation.*

385 • *Apply max pooling with a 2×2 pool size.*

386 • *Repeat the process with convolutional layers with 32 and 64 filters, each followed by max*
387 *pooling.*

388 • *Further apply three 2D convolutional layers with 128 filters each to capture higher-level*
389 *features.*

390 ➤ *CNN Branch 2*

391 • *Repeat the steps of CNN Branch 1, creating a similar structure with 16, 32, 64, and 128 filters.*

392 ➤ *Merge and Refinement*

393 • *After processing both branches separately, concatenate the feature maps from each branch*
394 *using 'Lambda' layers to compute the absolute difference at each level.*

395 • *Perform up-sampling and additional convolutions to progressively reconstruct the*
396 *segmentation mask.*

397 ➤ *Output Layer*

398 • *Apply a final 2D convolutional layer with a sigmoid activation to produce the output mask.*

399 *Step 3: Compile the Model*

400 • *Compile the model using Adam optimizer, learning rate of 1×10^{-4} and as the loss function*
401 *as binary cross-entropy. Set accuracy as the evaluation metric.*

402 *Step 4: Training and Evaluation*

403 *Step 5: Save the Model*

404

Table 3. Hyperparameters in the DSC-AD-SC model

Parameters	Values
Learning rate	0.0001
Loss	Binary cross entropy
Epoch	50
Batch size	2
Activation	ReLU
Optimizer	Adam

406

407 *2.4 Hardware and Software Setup*

408 The models were run on Google Collaboratory as the platform for the workstation. Google Colab
 409 enables one to write and run Python scripts, gratis usage of resources like GPUs and TPUs. Google
 410 Colab was chosen because it is flexible, user-friendly, and capable of parallel processing all of which
 411 are requirements for running deep learning models on large sets of data. Further, Colab's integration
 412 with Google Drive facilitates seamless data storage and recovery during model training and testing.
 413 The libraries, in addition to Python's extensive community support, provided the instruments
 414 necessary for quick model implementation, training, and testing. The Keras library was employed to
 415 develop the pieces, with TensorFlow being the backend. TensorFlow's flexibility and support for
 416 GPU enabled it to train the model efficiently, and Keras provided an easy way to describe the
 417 suggested architecture. Python, Google Colab, Keras, and TensorFlow offered a scalable and efficient
 418 framework for building and deploying the model.

419 **3. Results and Discussion**

420 The accuracy of the method for satellite image change detection is assessed by the Dice Similarity
 421 Score. It provides a quantitative measure of how accurately the model detects and marked areas of
 422 change between the two input images. The Dice score is computed as per Equation (18).

$$423 \text{ Dice score} = \frac{2 \times |X \cap Y|}{|X| + |Y|} \quad (18)$$

424 where X represents the predicted regions of change, and Y are the ground truth regions. The value
425 ranges from 0 to 1, with a higher score indicating better overlap. A Dice score of 1 denotes that the
426 model's prediction has perfectly overlapped with the ground truth, thereby indicating perfect accuracy
427 in the detection of changes. Taking areas of overlap into consideration allows for the counting of both
428 false positive (areas model wrongly identifies as change) and false negative (real change not
429 identified). Therefore, a high Dice score means that this model is efficiently capturing the true
430 changes and missing the wrong ones rather than the other two.

431 The improvements observed in the Dice similarity scores particularly for the DSC-AD-SC model
432 matches a recent study, which encourages the modeling of feature differences in such bi-temporal
433 change detection tasks. The same performance improvement has been achieved when leveraging
434 absolute difference-based fusion strategies to enhance sensitivity toward temporal variations in
435 satellite images (Mei et al., 2023; Kalinaki et al., 2023). Also, Shafique et al. (2022) proved that dual-
436 stream methods with shared encoder can achieve better performance with less complicated models.
437 According to the findings, the proposed approach is effective and capable of capturing the
438 environmental changes.

439 The AC-PF model's training accuracy as shown in Figure 9 reveals an initial increase in accuracy,
440 with validation accuracy consistently hovering around 96.80% over multiple epochs. By epoch 20,
441 the model achieved a stable accuracy of approximately 96.80%. As training progressed, accuracy
442 gradually improved, surpassing 97.50% by epoch 30, although validation accuracy remained stable
443 around 96.5%.

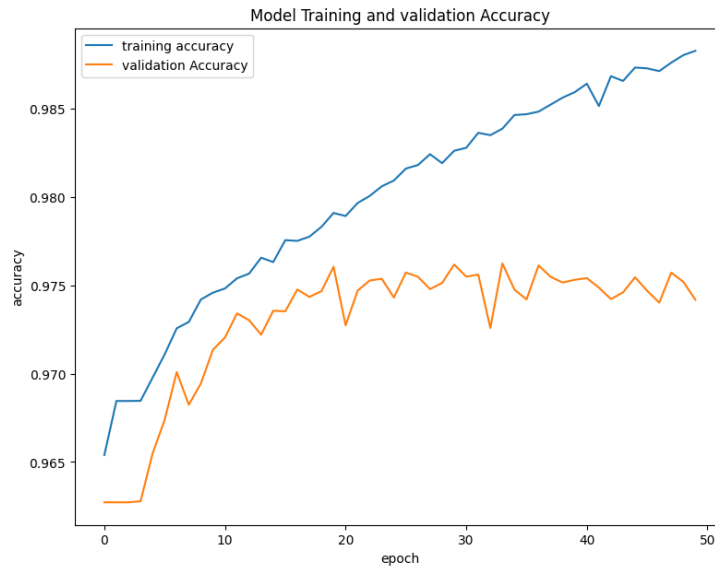


Figure 9. Accuracy plot of the AC-PF model

444

445

446 According to the training of the DSC-SC model shown in Figure 10, there is a sharp increase in
 447 accuracy followed by a stabilization phase. The validation accuracy during various epochs remained
 448 consistent at 95.20%. By epoch 15, the model achieved 96.10% accuracy. As training continued, the
 449 accuracy gradually improved, surpassing 96% by epoch 25. It can be observed that training loss
 450 reduced but validation loss fluctuated. This fluctuation indicates the model is suffering from
 451 overfitting.

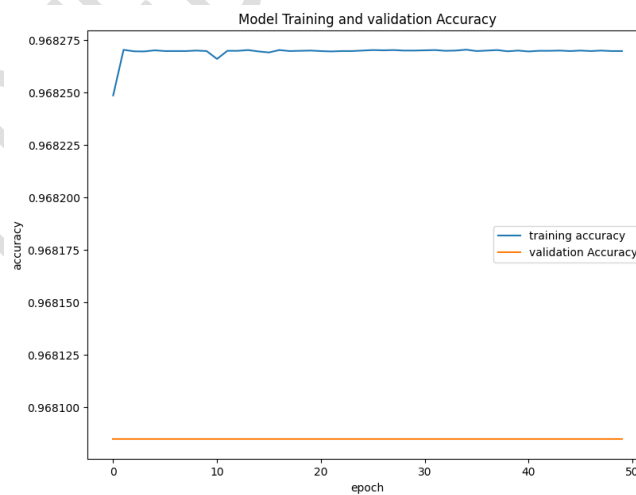


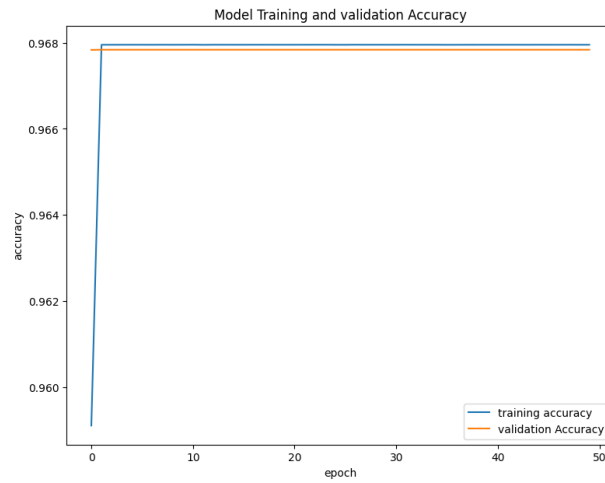
Figure 10. Accuracy plot of the DSC-SC model

452

453

454 The DSC-AD-SC model's training results, initially improved, as indicated in Figure 11, with
 455 validation accuracy remaining around 96.75% throughout many epochs. By epoch 10, the model
 456 achieved a consistent accuracy of about 96.75%. As training progressed, the model continued to

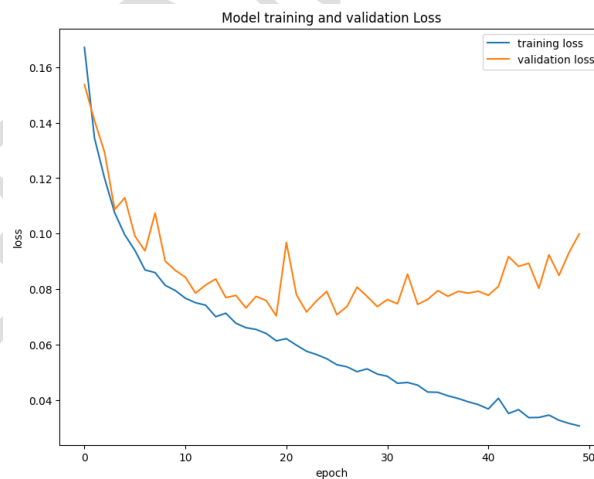
457 improve incrementally in accuracy, reaching values above 97% by epoch 30, while validation
458 accuracy remained close to 96.5%.



459

460 **Figure 11.** Accuracy plot of the model DSC-AD-SC model

461 The AC-PF model's loss, as exhibited in Figure 12, exhibited a steady decline in the initial training
462 epochs, indicating effective learning; however, it began to show signs of instability as training
463 advanced, particularly after it reached a lower threshold around 0.10. This instability became more
464 pronounced in the later epochs, where validation loss increased to approximately 0.15-0.17.

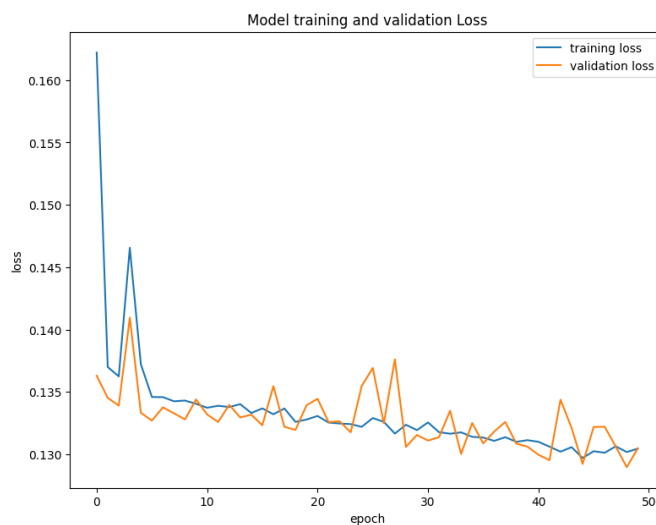


465

466 **Figure 12.** Loss plot of the AC-PF model

467 The DSC-SC system's loss exhibited a notable decline during the initial phases of training, as shown
468 in Figure 13, signifying effective learning and adaptation to the dataset. However, as training
469 progressed, the loss began to show irregular fluctuations, particularly after reaching a stabilization

470 point around 0.12. This variability became more pronounced in the later epochs, where validation
471 loss increased to values ranging from 0.16 to 0.19, indicating potential overfitting.



472

473 **Figure 13.** Loss plot of the model DSC-SC model

474 The DSC-AD-SC model's loss initially decreased, reflecting effective learning in the early training
475 stages, as shown in Figure 14, but began to fluctuate as training progressed, particularly after reaching
476 a lower threshold around 0.13 to 0.14. This fluctuation in validation loss, especially towards the later
477 epochs where it increased to 0.18–0.20, indicates that the model is experiencing some degree of
478 overfitting. As illustrated in Figures 9-11, all three models converge stably during training. In
479 addition, the DSC-AD-SC model achieves higher validation accuracy. The loss curves in Figures 12-
480 14 indicate effective learning behavior, although small fluctuations do suggest overfitting in the later
481 epochs. While some minor signs of overfitting were recognized during training, various measures
482 were taken to prevent it. The sample varieties were increased using the data augmentation so that the
483 models become less sensitive to spatial patterns. Furthermore, shared-weight encoders were used in
484 the dual-stream architectures to limit model complexity and encourage similar feature learning from
485 bi-temporal inputs. Validation performance was also monitored because training beyond convergence
486 was avoided to prevent over-optimization. Despite the small datasets, these strategies collectively
487 help limit overfitting.

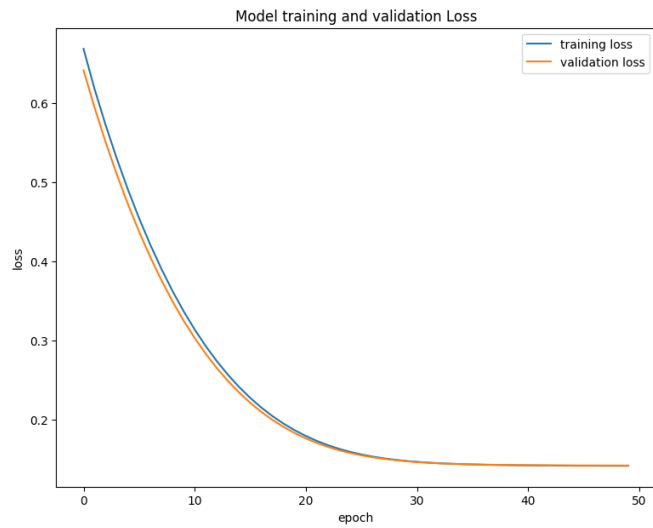


Figure 14. Loss plot of the DSC-AD-SC model

488

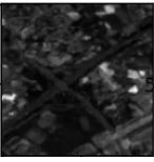
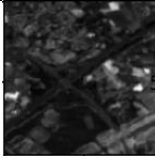
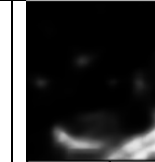
489

490 Table 4 presents the Dice similarity scores for various images in the AC-PF model. Figure 15 shows
 491 the visualization of these images.

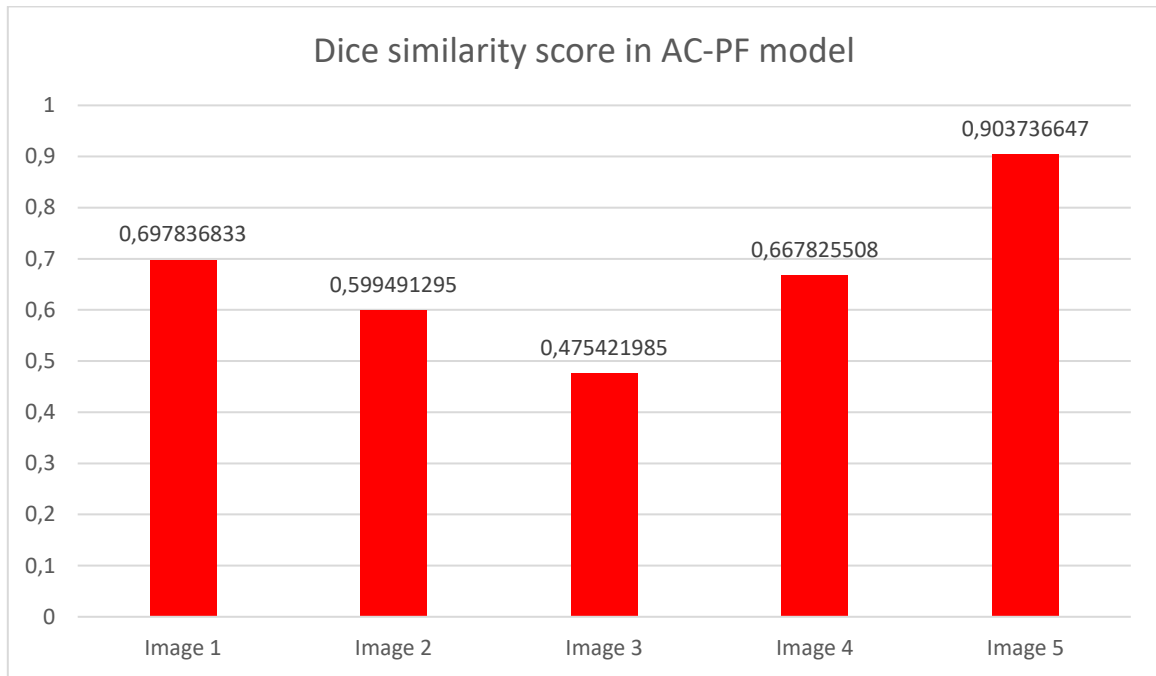
492

Table 4. Dice similarity score calculation in AC-PF model

Image	Initial Image	Changed Image	Ground Truth	Prediction	Dice Similarity Score
Image 1					0.6978368327274562
Image 2					0.59949129493561
Image 3					0.4754219845073826
Image 4					0.6678255080203945

Image 5					0.9037366465587999
---------	---	---	---	--	--------------------

493



494

Figure 15. Dice similarity score of different images in AC-PF model

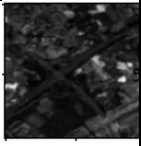
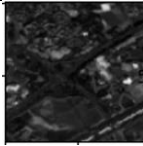
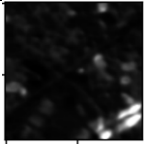
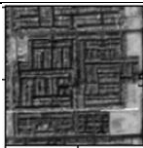
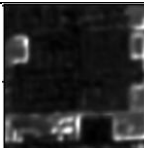
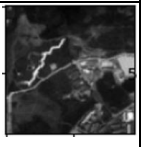
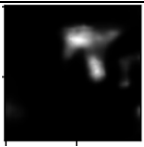
495

496 Table 5 presents the Dice similarity scores for various images in the DSC-SC model. Figure 16 shows
 497 the visualization of these images.

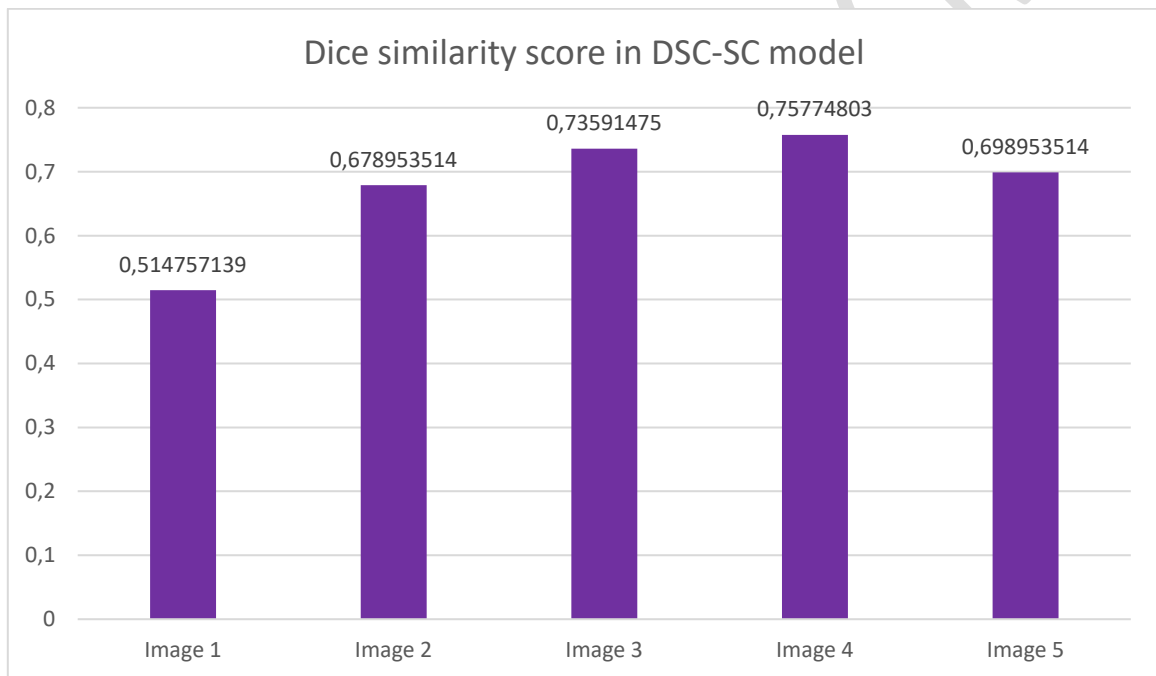
498

Table 5. Dice similarity score calculation in DSC-SC model

Image	Initial Image	Changed Image	Ground Truth	Prediction	Dice Similarity Score
Image 1					0.5147571393047798
Image 2					0.6789535143347377

Image 3					0.7359147499259855
Image 4					0.7577480297543387
Image 5					0.6989535143347377

499



500

501

Figure 16. Dice similarity score of different images in DSC-SC model

502

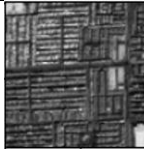
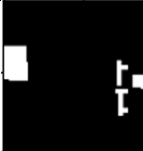
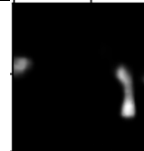
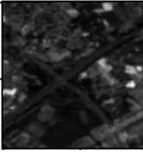
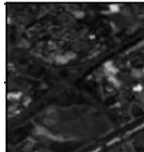
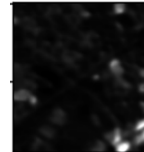
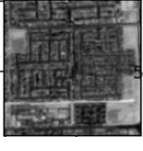
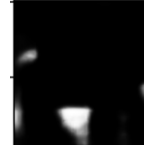
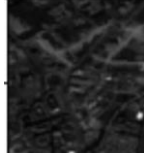
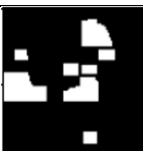
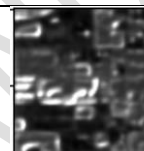
Table 6 presents the Dice similarity scores for various images in the DSC-AD-SC model. Figure 17 shows the visualization of these images. A comparative analysis of Tables 4-6 highlights that the DSC-AD-SC model consistently outperforms the other architectures across most test images, confirming the benefit of incorporating absolute difference-based feature fusion for change detection.

505

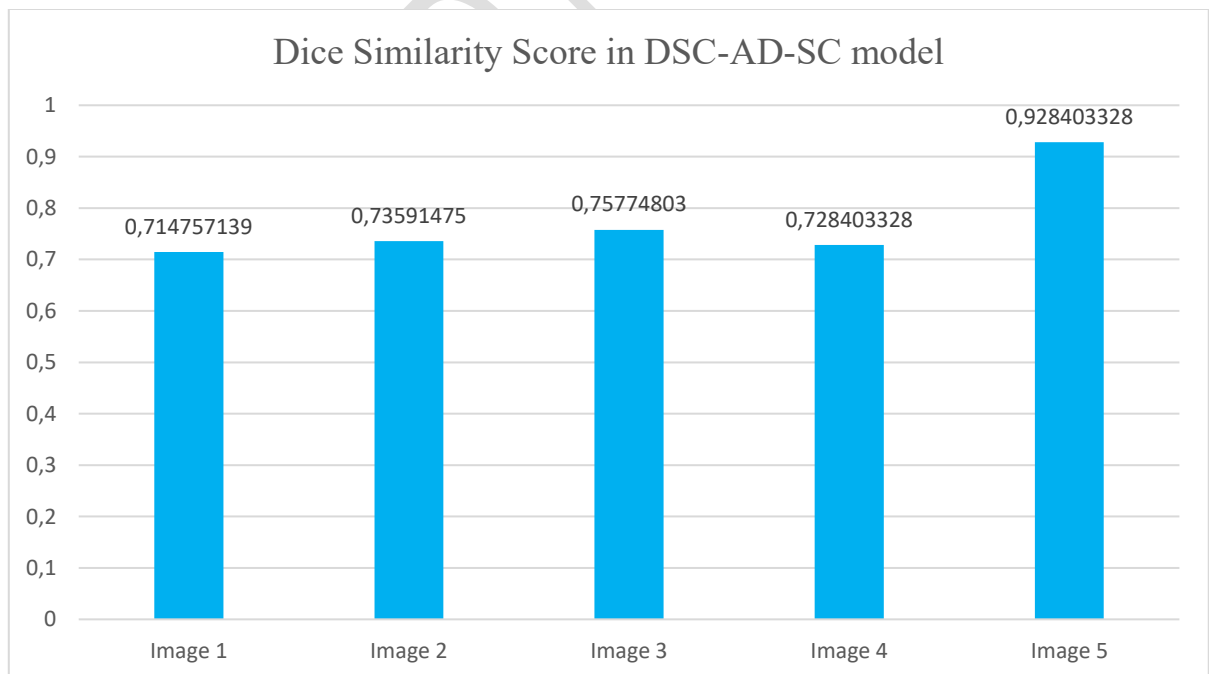
506

Table 6. Dice similarity score calculation in DSC-AD-SC model

Image	Initial Image	Changed Image	Ground Truth	Prediction	Dice Similarity Score
-------	---------------	---------------	--------------	------------	-----------------------

Image 1					0.7147571393047798
Image 2					0.7359147499259855
Image 3					0.7577480297543387
Image 4					0.7284033284077162
Image 5					0.9284033284077162

507



508

509

Figure 17. Dice similarity score of different images in DSC-AD-SC model

510 Although the Dice Similarity Score is a useful quantitative measure for comparing segmentation
511 performance, the current study does not perform formal significance testing or confidence interval
512 estimation. Incorporating repetitions of such analyses across a few runs and datasets would enhance
513 the robustness of the claims. This is an important direction for future work, particularly for the large-
514 scale deployment and benchmarking of change detection models.

515 In real-time environmental monitoring applications, false positives and false negatives have different
516 effects. When change is not detected, false positives cause unnecessary allocation (e.g., inspecting or
517 intervening). On the other hand, false negatives are much more damaging, as they could mean missing
518 significant environmental changes like deforestation, urban encroachment, and damage from
519 disasters. The DSC-AD-SC model proposed here is designed to additionally raise the sensitivity to
520 actual temporal variations while maintaining the spatial coherence in a model that is less likely to
521 suffer from any of the two failures.

522 **4. Conclusion**

523 Accurate and reliable change detection using satellite imagery plays a crucial role in understanding
524 environmental dynamics related to urbanization, deforestation, and natural disasters. This study
525 investigated three deep learning-based change detection architectures: DSC-SC, AC-PF, and the
526 proposed DSC-AD-SC using the Onera Satellite Change Detection Dataset. Experimental results
527 demonstrated that incorporating absolute difference-based skip connections within a dual-stream
528 framework significantly improves change localization performance. Among the evaluated methods,
529 the DSC-AD-SC model achieved the highest Dice Similarity Score, indicating its effectiveness in
530 capturing meaningful temporal changes while preserving spatial detail.

531 Besides quantitative performance, the study shows that architectural design choices can remedy the
532 limitations observed in conventional methods for change detection. The method proposed effectively
533 increases the sensitivity to actual changes in the environment such as land-cover change and disaster
534 assessment by modeling the differences that exist at the feature level between two temporal images.

535 The deployment of change detection systems that use deep learning will face challenges in the real
536 world. When processing a large number of high-resolution satellite images, scalability may be
537 hampered due to high computational requirements. In addition, access to properly labeled and
538 temporally aligned datasets is often limited, which can affect practical deployment. Changes in sensor
539 settings, seasonal conditions, and acquisition settings may influence model generalization further,
540 necessitating caution before operational use.

541 In the future, these challenges will be addressed through computationally efficient model
542 architectures and improved training strategies. Integrating multispectral and SAR data and other data
543 types is a promising way forward to achieving robustness in various conditions. In addition, expand
544 the evaluation to include a larger set of data, and performing statistical significance testing based on
545 multiple runs can increase confidence in the application of the proposed framework for longer
546 environmental monitoring and decision support.

547

548 During the preparation of this work, the author(s) used Microsoft Word, Grammarly and
549 <https://www.drawio.com/> in order to improve grammar, enhance language clarity and design
550 technical diagrams. After using these tools/services, the author(s) reviewed and edited the content as
551 needed and take full responsibility for the content of the publication.

552 **References**

553 Arowolo A.O. and Deng X. (2018), Land use/land cover change and statistical modelling of cultivated
554 land change drivers in Nigeria, *Regional Environmental Change*, **18**, 247-259.

555 Asokan A. and Anitha J.J. (2019), Change detection techniques for remote sensing applications: A
556 survey, *Earth Science Informatics*, **12**, 143-160.

557 Degife A., Worku H., Gizaw S. and Legesse A. (2019), Land use land cover dynamics, its drivers and
558 environmental implications in Lake Hawassa Watershed of Ethiopia, *Remote Sensing
559 Applications: Society and Environment*, **14**, 178-190.

560 Goswami A., Sharma D., Mathuku H., Gangadharan S.M.P., Yadav C.S., Sahu S.K. et al. (2022),
561 Change detection in remote sensing image data comparing algebraic and machine learning
562 methods, *Electronics*, **11**, 431.

563 Han Y., Javed A., Jung S. and Liu S. (2020), Object-based change detection of very high resolution
564 images by fusing pixel-based change detection results using weighted Dempster–Shafer theory,
565 *Remote Sensing*, **12**, 983.

566 Ibtehad N. and Rahman M.S. (2020), MultiResUNet: Rethinking the U-Net architecture for
567 multimodal biomedical image segmentation, *Neural Networks*, **121**, 74-87.

568 Kalinaki K., Malik O.A. and Lai D.T.C. (2023), FCD-AttResU-Net: An improved forest change
569 detection in Sentinel-2 satellite images using attention residual U-Net, *International Journal of*
570 *Applied Earth Observation and Geoinformation*, **122**, 103453.

571 Kalinicheva E., Ienco D., Sublime J. and Trocan M. (2020), Unsupervised change detection analysis
572 in satellite image time series using deep learning combined with graph-based approaches, *IEEE*
573 *Journal of Selected Topics in Applied Earth Observations and Remote Sensing*, **13**, 1450-1466.

574 Khankeshizadeh E., Mohammadzadeh A., Moghimi A. and Mohsenifar A. (2022), FCD-R2U-net:
575 Forest change detection in bi-temporal satellite images using the recurrent residual-based U-net,
576 *Earth Science Informatics*, **15**, 2335-2347.

577 Kumar S., Meena R.S., Sheoran S., Jangir C.K., Jhariya M.K., Banerjee A. and Raj A. (2022), Remote
578 sensing for agriculture and resource management, In: *Natural Resources Conservation and*
579 *Advances for Sustainability*, Elsevier, 91-135.

580 Liu T., Yang L. and Lunga D. (2021), Change detection using deep learning approach with object-
581 based image analysis, *Remote Sensing of Environment*, **256**, 112308.

582 Mei J., Zheng Y.B. and Cheng M.M. (2023), D2ANet: Difference-aware attention network for multi-
583 level change detection from satellite imagery, *Computational Visual Media*, **9**, 563-579.

584 Sefrin O., Riese F.M. and Keller S. (2020), Deep learning for land cover change detection, *Remote*
585 *Sensing*, **13**, 78.

- 586 Shafique A., Cao G., Khan Z., Asad M. and Aslam M. (2022), Deep learning-based change detection
587 in remote sensing images: A review, *Remote Sensing*, **14**, 871.
- 588 Shi W., Zhang M., Zhang R., Chen S. and Zhan Z. (2020), Change detection based on artificial
589 intelligence: State-of-the-art and challenges, *Remote Sensing*, **12**, 1688.
- 590 Song A., Kim Y. and Han Y. (2020), Uncertainty analysis for object-based change detection in very
591 high-resolution satellite images using deep learning network, *Remote Sensing*, **12**, 2345.
- 592 Tahir A., Munawar H.S., Akram J., Adil M., Ali S., Kouzani A.Z. and Mahmud M.P. (2022),
593 Automatic target detection from satellite imagery using machine learning, *Sensors*, **22**, 1147.
- 594 Tanim A.H., McRae C.B., Tavakol-Davani H. and Goharian E. (2022), Flood detection in urban areas
595 using satellite imagery and machine learning, *Water*, **14**, 1140.
- 596 Walter V. (2004), Object-based classification of remote sensing data for change detection, *ISPRS*
597 *Journal of Photogrammetry and Remote Sensing*, **58**, 225-238.